nature ecology & evolution

SUPPLEMENTARY INFORMATION

DOI: 10.1038/s41559-017-0287-3

In the format provided by the authors and unedited.

Environmental structuring of marine plankton phenology

Daniel G. Boyce[1,2]*, Brian Petrie[2], Kenneth T. Frank[2], Boris Worm[3] and William C. Leggett[1]

[1]Department of Biology, Queen's University, Kingston, ON K7L 3N6, Canada. [2]Ocean Sciences Division, Bedford Institute of Oceanography, PO Box 1006, Dartmouth, NS B2Y 4A2, Canada. [3]Department of Biology, Dalhousie University, Halifax, NS B3H 4R2, Canada. *e-mail: Dgb1@queensu.ca

Supporting Information (SI): Environmental structuring of marine plankton phenology

Daniel G. Boyce, Brian Petrie, Kenneth T. Frank, Boris Worm, & William C. Leggett

Contents

Phytoplankton data

We assembled a database of all publicly available indices of surface ocean phytoplankton biomass concentration derived from ship-based and remote sensing observation platforms available between 1995 and 2015. The observations were extracted at the highest spatial and temporal resolutions possible (Table S1).

Shipboard in situ observations of Chl or calibrated Chl

We used a publicly-available database of integrated chlorophyll values (Chl) collected via shipboard sampling platforms (details in Boyce *et al.*, 2012[1]). The calibrated Chl values in the database were derived from measurements of ocean transparency (derived from Secchi-depth measurements; ZD) and colour (derived from the Forel-Ule color-matching scale; FU), which were both calibrated against a comprehensive database of quality-controlled *in situ* Chl measurements derived from spectrophotometric or fluorometric analyses of seawater. Full details of this database, including the data sources, temporal and geographic distribution, quality control and inter-calibration are described in Boyce *et al.* (2012)[1].

Chlorophyll measurements sourced from the International Council for the Exploration of the Sea (ICES), and Canadian Department of Fisheries and Oceans (DFO) BIOCHEM databases were also used. Measurements from these databases that were already contained in the Boyce *et al.* (2012) database were removed prior to the analysis; Chl measurements were then averaged over the ocean's upper 20 m.

Remote sensing observations of Chl

Measurements of Chl derived from remotely sensed ocean leaving radiances were extracted from the National Aeronautics and Space Administration's (NASA) ocean colour database. Chl measurements derived from the Coastal Zone Color Scanner[2] (CZCS; 1978-1986), and the Sea-viewing Wide Field of view Sensor[3] (SeaWiFS; 1997-2010), Moderate-resolution Imaging spectroradiometer (MODIS; 2003-

2014), and Medium-resolution imaging spectrometer (MERIS; 2002-2012) were used. These Chl estimates were extracted at the highest temporal resolution possible (1 or 8 days). At each time point, Chl measurements were spatially interpolated to 1° x 1° cells using nearest neighbor algorithms.

Continuous plankton recorder observations of ocean colour

Semi-quantitative estimates of ocean colour derived from the continuous plankton recorder (CPR) across the Northwest Atlantic were acquired from the Canadian Department of Fisheries and Oceans (DFO) and the National Ocean and Atmospheric Administration (NOAA). The CPR is towed behind volunteer vessels at a depth of 5-10 m, and colour samples are obtained as seawater flows through a 270 µm micron silk mesh within the instrument[4]. Each CPR sample is compared to a standardized colour chart and recorded on a phytoplankton colour index scale (PCI) ranging from 0 (no green) to 3 (green). Experiments have shown that these PCI categories represent a semi-logarithmic scale of increasing colour intensity such that PCI 2 samples have twice as much colour as PCI 1, and PCI 3 samples 6.5 times as much as PCI 1[ref. 5]. PCI estimates are available in the Northwest Atlantic since 1957.

Simulation analyses

The number of measurements required to accurately resolve the full spectrum of phenological variability within the global oceans was determined through simulation analyses. Three phenocycles were simulated to approximate those observed in the ocean, in terms of modality, amplitude, and periodicity[6–8]. To these simulated trends, we added Gaussian distributed white noise:

$$\mathrm{N}(\mu, \sigma^2)$$

where μ is the mean, set to 0, and σ^2 is the standard deviation, set to 0.18 or 0.54, respectively. These variances correspond to 100 or 300% of the upper 99th percentile of all phenocycle$_{G,D}$ variances estimated using global field observations. The average standard deviation of all of the phenocycles$_{G,D}$ estimated from the database was 0.013, and 99% of the standard deviations were less than 0.18.

Therefore, the levels of variability for the simulated phenocycles (σ^2) were conservatively set 100% and 300% higher than any estimated in the ocean. Each of these 6 simulated phenocycles, was iteratively sub-sampled to obtain sample sizes ranging from 6 to 75 in steps of 1, with 100 replicates each. For each subsample (n=6900), a phenocycle was estimated using equation 1, and the similarity between the recovered and "true" phenocycles was quantified (Supplementary Figs. 2 & 3). For each iteration, the difference between the strength (amplitude) and timing (phase) of the recovered and true phenocycle was calculated, as was the linear dependence (Pearson r). The recovered phenocycles were also iteratively substituted into the fuzzy clustering analysis of the global phenocycles. This process enabled us to quantitatively determine the minimum data availability criteria needed to accurately recover the "true" phenocycle under different levels of variability.

The simulation revealed that long stretches of missing observations had the strongest univariate effect on the ability of our approach to accurately recover the true phenocycle, but that the number of available months of observations was also important. Cumulatively, the simulation analysis indicated that a minimum of 8 months of observations, with no more than 75 consecutive missing days were required for accurate phenocycle estimation. At these levels, the probability of correct phenocycle clustering ranged from 88% to 100% and the correlation between the recovered and true phenocycle ranged from 0.94 to 1 when σ^2= 0.18.

Distance decorrelation

GAMs were used to estimate the distance decay scale of phytoplankton phenocycles$_A$ within each grid cell as

$$\hat{r} = \beta_0 + f_1(Distance_i) + \varepsilon_i, \quad (1)$$

where *i* are the individual observations, $\hat{r}$ is the expected correlation between phenocycles$_A$, $Distance_i$ is the great circle distance (km) between the phenocycles$_A$, β_0 is the model intercept, f_1 denotes the functional effect estimated from the data, and ε_i represents the residual error term. The functional effect

in the model allows the correlation between all phenocycles$_A$ to be estimated as a continuous, cyclic smooth function of the omnidirectional distance between them. As a sensitivity check on our use of the GAM approach, distance decorrelation was also estimated using an exponential decay model[9,10]. The exponential decay model was estimated within each grid cell as

$$\hat{r} = \beta_0 e^{-vDistance_i}, \quad (2)$$

where *i* are the individual observations, $\hat{r}$ is the expected correlation between phenocycles$_A$, $Distance_i$ is the great circle distance (km) between the phenocycles$_A$, β_0 is the model intercept, and v is the *e*-folding scale. The equation was estimated using non-linear least squares. We fitted models where the intercept was fixed at 1 or estimated from the data. Estimated decorrelation distances produced using these two approaches were very similar (r=0.64), and the spatial patterns of decorrelation being virtually identical (Supplementary Fig. 7).

We also estimated the symmetry and directionality of decorrelation. To quantify the symmetry of decorrelation in zonal and meridional axes, we estimated the distance decorrelation scale along strictly longitude directions (holding latitude fixed) and strictly latitudinal directions (holding longitude fixed) for each individual grid cell. To avoid non-linear patterns in the distance to correlation relationships, the maximum distances considered in each instance was set to 8000 kms, the maximum empirically estimated distance. For each grid cell, we scaled the decorrelation distances in longitude and latitude directions to the maximum decorrelation distance estimated for that cell. In this manner, instances where the decorrelation distance were similar along longitudinal and latitudinal directions received were more symmetric (Supplementary Fig. 9). To estimate the directionality of phenological decorrelation, scales were estimated in cardinal directions (north, east, south, and west), and scaled in the same manner described above, for zonal and meridional decorrelations. In this manner, the symmetry and direction of the decorrelation distances were derived (Supplementary Fig. 10).

Supplementary References

1. Boyce, D. G. D. G., Lewis, M. & Worm, B. Integrating global chlorophyll data from 1890 to 2010. *Limnol. Oceanogr. Methods* **10,** 840–852 (2012).
2. Hovis, W. A. *et al.* Nimbus-7 coastal zone color scanner: system description and initial imagery. *Science* **210,** 60–63 (1980).
3. McClain, C. R., Feldman, G. C. & Hooker, S. B. An overview of the SeaWiFS project and strategies for producing a climate research quality global ocean bio-optical time series. *Deep. Res. II* **51,** 5–42 (2004).
4. Batten, S. D. *et al.* CPR sampling: the technical background, materials and methods, consistency and comparability. *Prog. Oceanogr.* **58,** 193–215 (2003).
5. Warner, A. J. & Hays, G. C. Sampling by the continuous plankton recorder survey. *Prog Ocean.* **34,** 237–256 (1994).
6. Racault, M. F., Le Quéré, C., Buitenhuis, E., Sathyendranath, S. & Platt, T. Phytoplankton phenology in the global ocean. *Ecol. Indic.* **14,** 152–163 (2012).
7. Sapiano, M. R. P., Brown, C. W., Schollaert Uz, S. & Vargas, M. Establishing a global climatology of marine phytoplankton phenological characteristics. *J. Geophys. Res. Ocean.* **117,** 1–16 (2012).
8. D'Ortenzio, F., Antoine, D., Martinez, E. & Ribera d'Alcalà, M. Phenological changes of oceanic phytoplankton in the 1980s and 2000s as revealed by remotely sensed ocean-color observations. *Global Biogeochem. Cycles* **26,** 1–16 (2012).
9. Frank, K. T., Petrie, B., Leggett, W. C. & Boyce, D. G. Large scale, synchronous variability of marine fish populations driven by commercial exploitation. *Proc. Natl. Acad. Sci.* 201602325 (2016). doi:10.1073/pnas.1602325113
10. Myers, R. A., Mertz, G. & Barrowman, N. J. Spatial scales of variability in cod recruitment in the

North Atlantic. *Can. J. Fish. Aquat. Sci.* **52,** 1849–1862 (1995).

11. Hartigan, J. A. & Hartigan, P. M. The dip test of unimodality. *Ann. Stat.* **13,** 70–84 (1985).

Supplementary Tables

Supplementary Table 1 | Data sources.

Database	Metric	Platform	Region	Years	Depth	Type	Source
Boyce et al. 2012	Chl	*In situ*	Global	1995-2010	<20 m	1	www.onlinelibrary.wiley.com/doi/10.4319/lom.2012.10.840/full
ICES	Chl	*In situ*	Atlantic	1995-2015	<20 m	1	www.ices.dk/marine-data/dataset-collections/Pages/default.aspx
BIOCHEM	Chl	*In situ*	Atlantic	1995-2015	<20 m	1	www.dfo-mpo.gc.ca/science/data-donnees/biochem
Palmer Station	Chl	*In situ*	Antarctica	1995-2015	<20 m	1	www.pal.lternet.edu/
MODIS	Chl	Satellite	Global	2003-2014	~20 m*	2	www.oceandata.sci.gsfc.nasa.gov/
SeaWiFS	Chl	Satellite	Global	1997-2010	~20 m*	2	www.oceandata.sci.gsfc.nasa.gov/
MERIS	Chl	Satellite	Global	2002-2012	~20 m*	3	www.oceandata.sci.gsfc.nasa.gov/
CPR (NOAA)	Colour	Underway	NW Atlantic	1995-2010	10 m	4	www.nefsc.noaa.gov/epd/ocean/MainPage/ios.html
CPR (SAHFOS)	Colour	Underway	N Atlantic	1995-2013	10 m	4	www.sahfos.ac.uk/
CPR (SAHFOS)	individuals	Underway	NW Atlantic	1995-2013	10 m	1	www.sahfos.ac.uk/
CPR (NPAC)	individuals	Underway	N Pacific	1997-2015	10 m	1	www.pices.int/projects/tcprsotnp/default.aspx/
CPR (SOUTH)	individuals	Underway	Southern	1995-2015	10 m	1	www.data.aad.gov.au/aadc/cpr/
CPR (AUS)	individuals	Underway	Australia	2007-2015	10 m	1	www.imos.org.au/australiancontinuousplanktonr0.html
COPEPOD	Carbon mass	Various	Global	1995-2015	<20 m	2	www.st.nmfs.noaa.gov/copepod/atlas/index.html
NOAA STAR	NDVI	Satellite	Global	1995-2015		NA	www.star.nesdis.noaa.gov/smcd/emb/vci/VH/vh_ftp.php
AVHRR Pathfinder	SST	Satellite	Global	1995-2015		NA	www.nodc.noaa.gov/SatelliteData/pathfinder4km/
AVHRR Pathfinder	Wind speed	Satellite	Global	1995-2015		NA	www.nodc.noaa.gov/SatelliteData/pathfinder4km/
MODIS	Cloud fraction	Satellite	Global	2002-2016		NA	www.neo.sci.gsfc.nasa.gov/
NODC WOA	Nitrate	Various	Global	1995-2015		NA	www.nodc.noaa.gov/OC5/woa13/
MET	Temperature	Various	Global	1995-2015		NA	www.metoffice.gov.uk/hadobs/
MET	Salinity	Various	Global	1995-2015		NA	www.metoffice.gov.uk/hadobs/

*Note: depth varies according to optical depth, which is spatially and seasonally variable.

Supplementary Figures

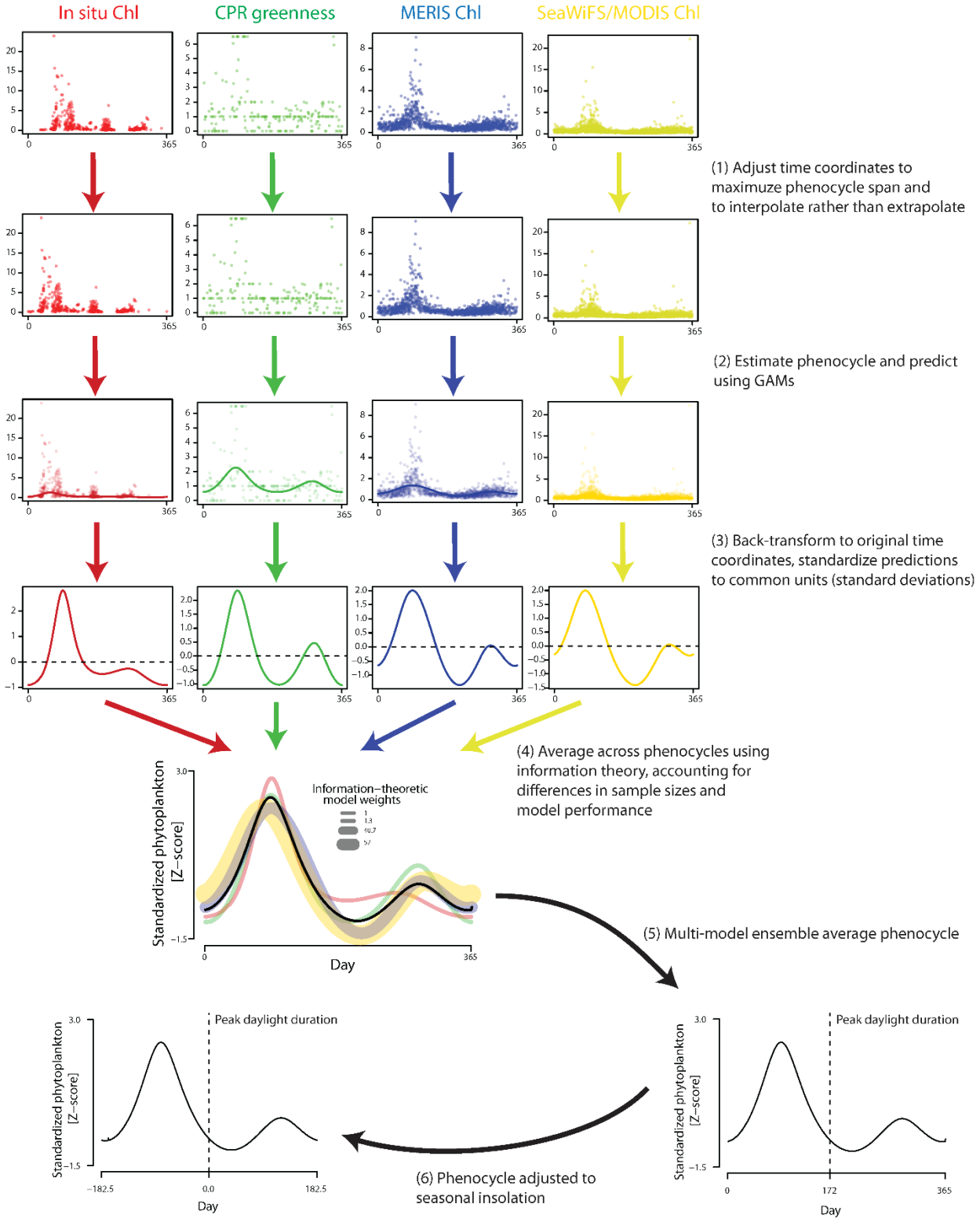

Supplementary Figure 1 | Illustrative example depicting how the phenocyclesA were estimated. Example was taken from grid cell in the NW Atlantic (longitude=-59.32; latitude=43.56).

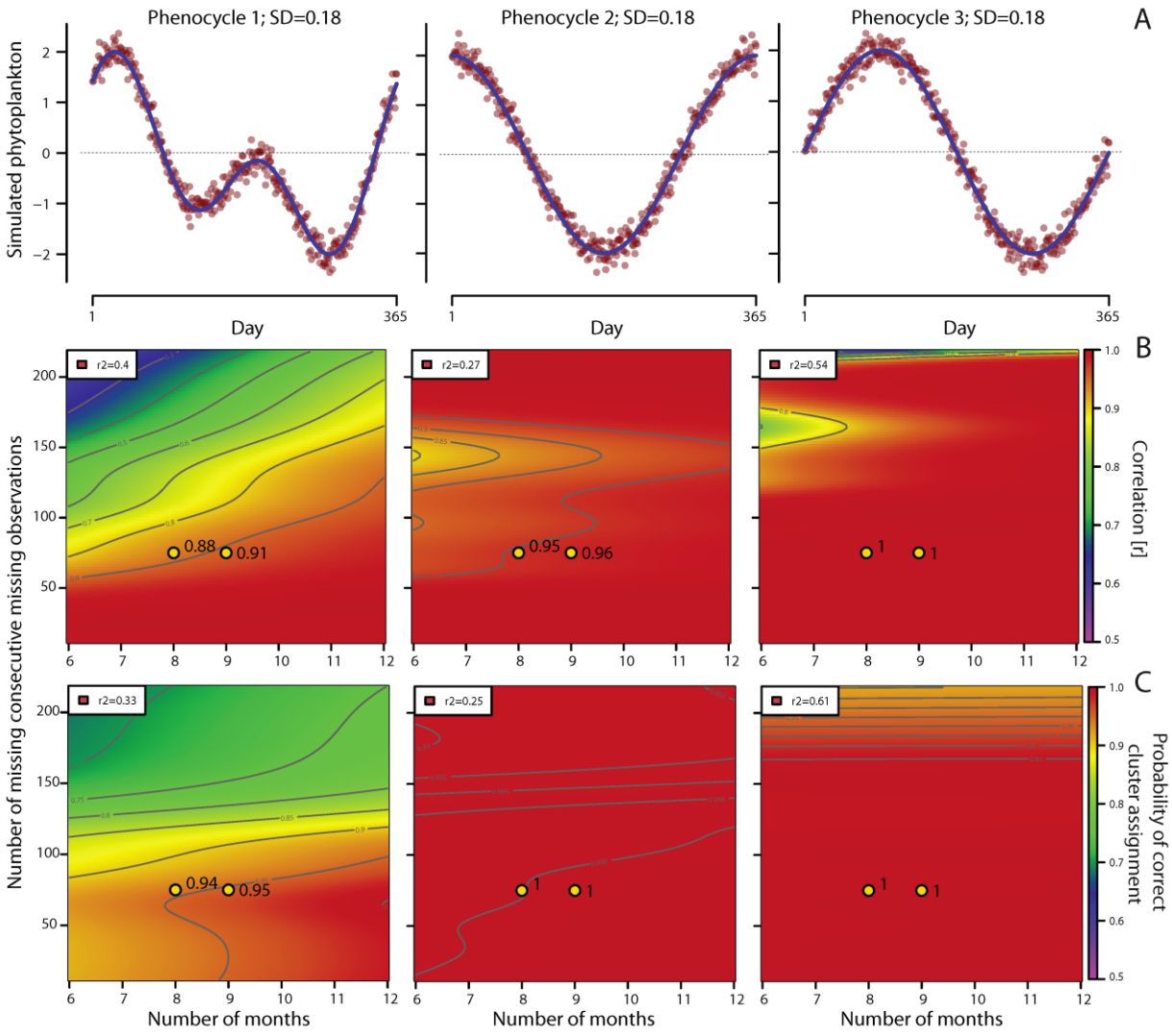

Supplementary Figure 2 | Simulated phenocycles. (A) Simulated phenocycle patterns with Gaussian white noise added (sd=0.18). (B-C) Agreement between simulated 'true' and estimated phenocycles under different sample sizes, number of available months (x-axes) and number of consecutive missing observations (y-axes). (B) Pearson correlation coefficient. (C) Probability of correct cluster assignment.

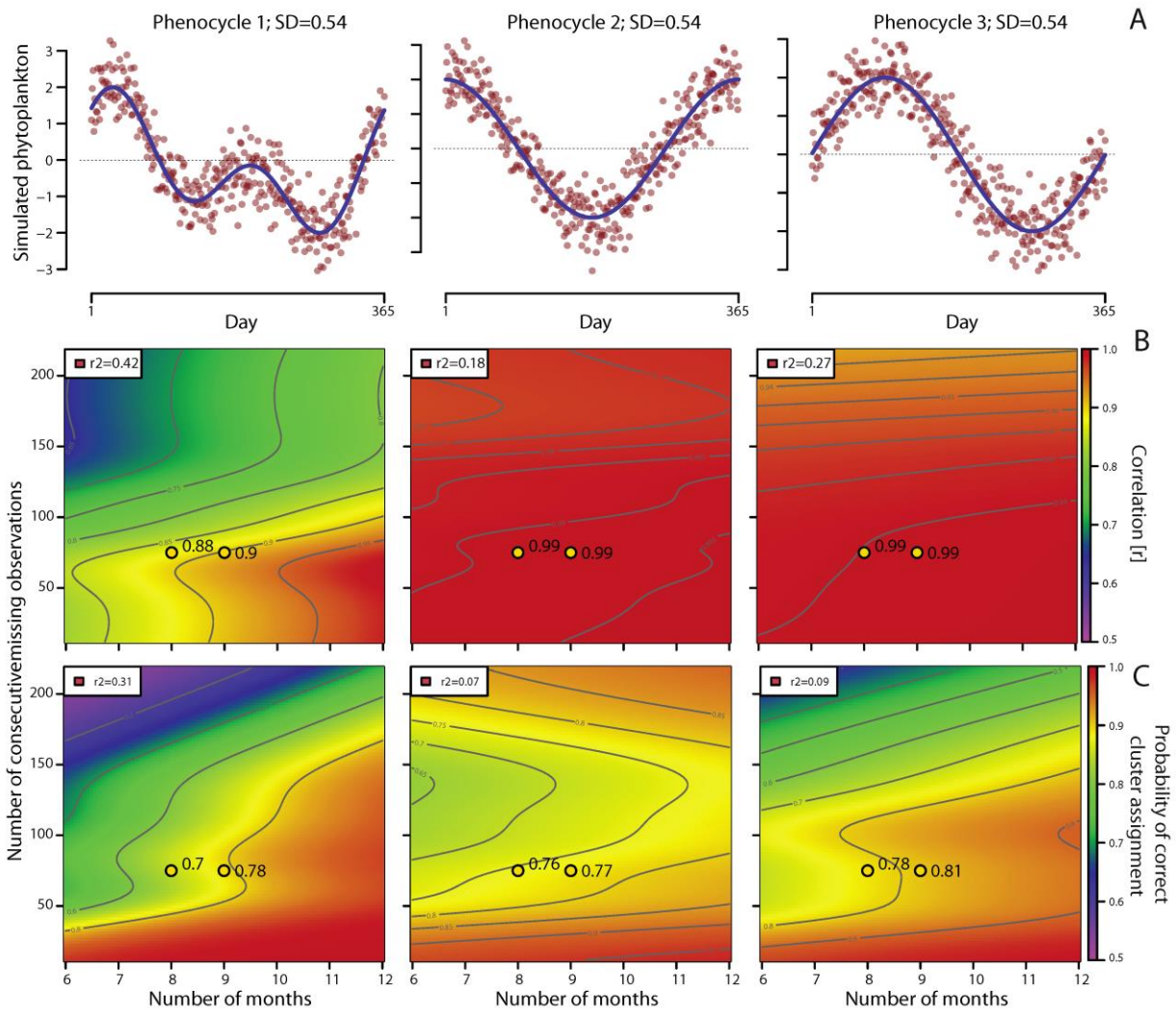

Supplementary Figure 3 | Simulated phenocycles. (A) Simulated phenocycle patterns with Gaussian white noise added (sd=0.54). (B-C) Agreement between simulated 'true' and estimated phenocycles under different sample sizes, number of available months (x-axes) and number of consecutive missing observations (y-axes). (B) Pearson correlation coefficient. (C) Probability of correct cluster assignment.

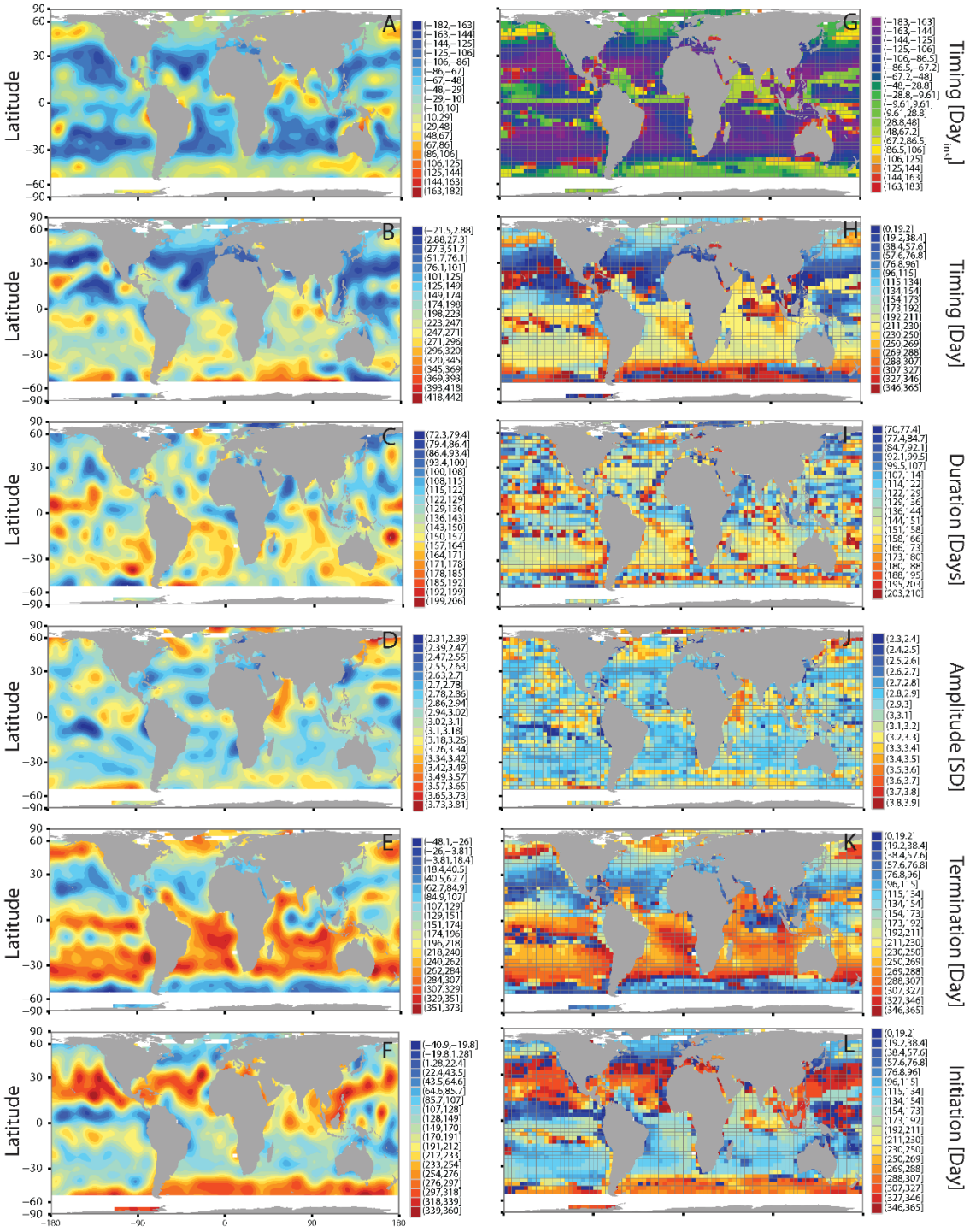

Supplementary Figure 4 | Indicators of marine phytoplankton phenology. (A,G) Insolation adjusted timing of maximum (B,H) timing of maximum (C,I) Duration of period of maximum (D,J) Amplitude (E,K) Timing of termination (F,L) Timing of initiation. Left columns are spatially interpolated and right columns are non-interpolated. Colours depict the magnitude of the response; dark blue depicts low values and dark red high.

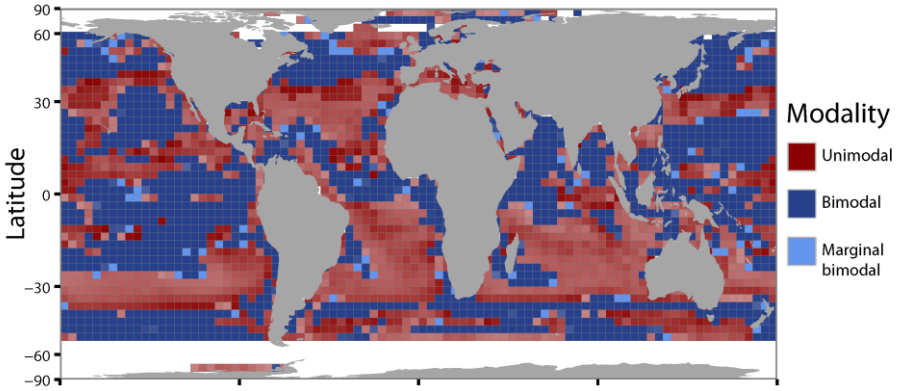

Supplementary Figure 5 | Modality of phytoplankton phenology. Probability of unimodality was estimated within each individual grid cell using Hartigan's dip test for unimodality[11]. Colours depict the identity of unimodal (single peak – red) or bimodal (two peaks – blue) phenology cycles for each cell. The light blue denotes marginal bimodality. The transparency of the colours depicts the certainty of the modality estimate.

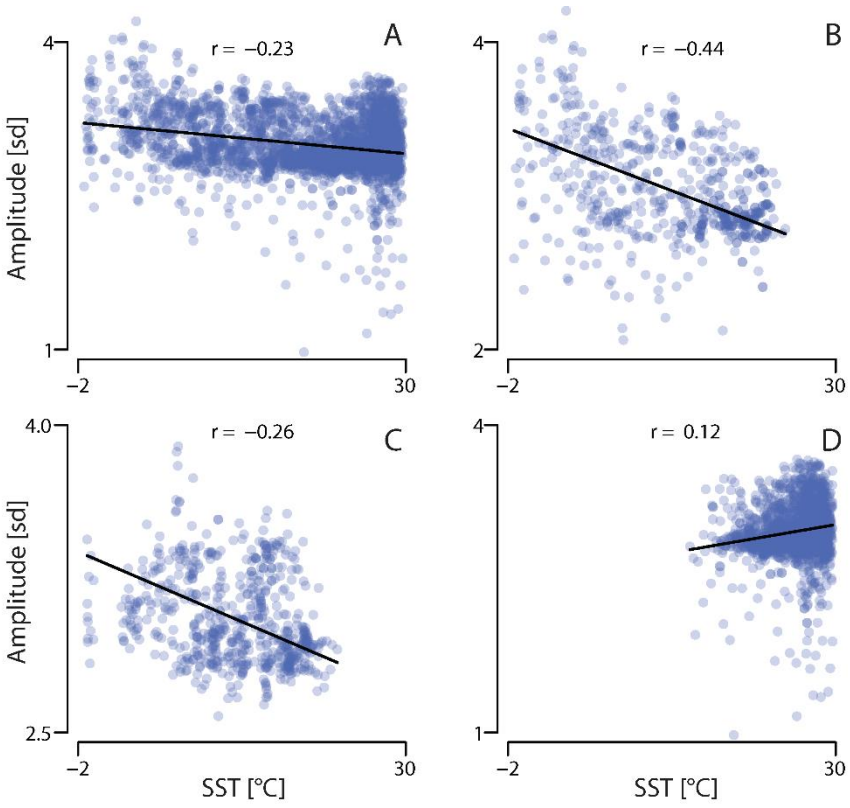

Supplementary Figure 6 | Relationship between average SST and the amplitude of phenology (A) globally, (B) within northern high latitude cells (>30°N), (C) southern high latitude cells (>30°S), and (D) equatorial cells (<30°N and S).

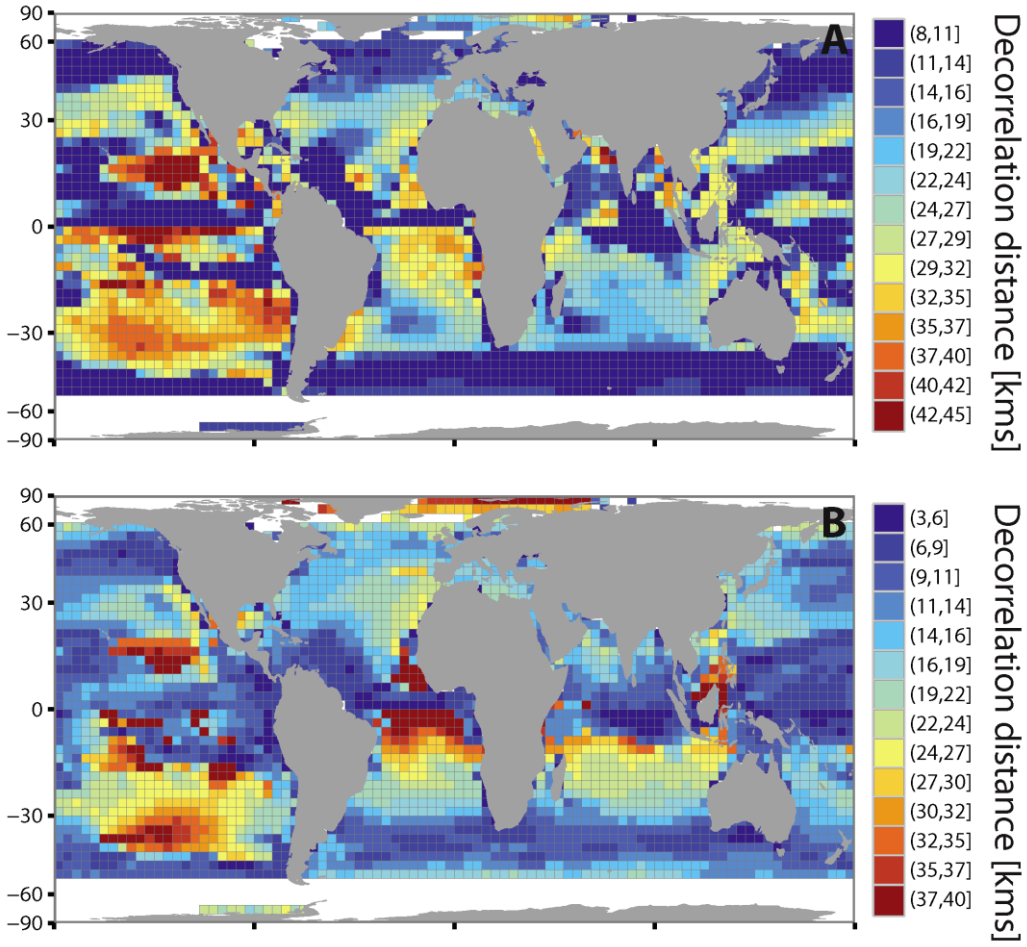

Supplementary Figure 7 | Distance decorrelation scales. Decorrelation scales estimated using (A) GAMs, (B) exponential decay models.

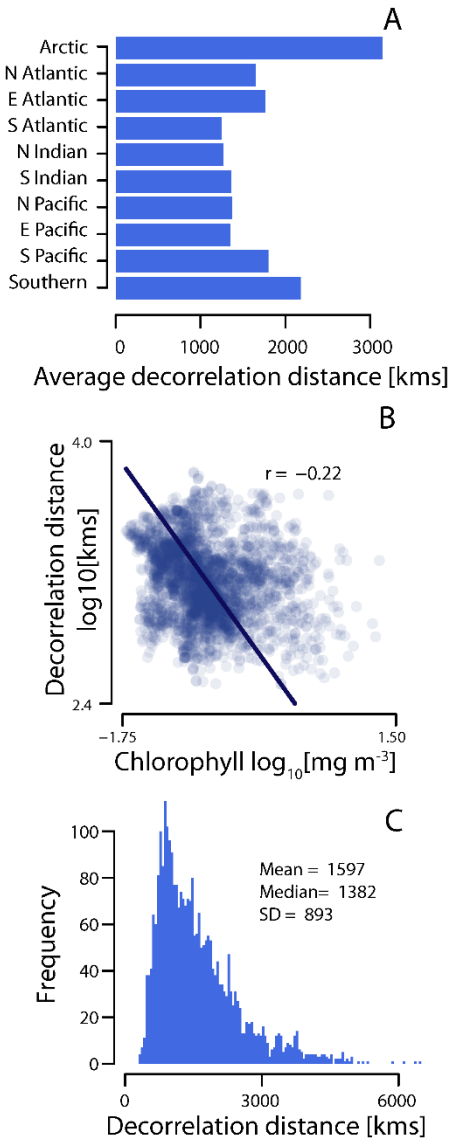

Supplementary Figure 8 | Patterns in estimated distance decorrelation scales of phytoplankton phenology. (A) Average estimated distance decorrelation of phytoplankton phenology for each of 10 large ocean regions over which phenology is commonly assumed to be uniform. (B) Linear relationship between the average upper ocean chlorophyll (mg m-3) and the distance decorrelation scale of phytoplankton phenology per equal area grid cell. Line is best fitting model II ranged major axis linear regression trend line. (C) Frequency distribution of all estimated phytoplankton phenology decorrelation scales globally.

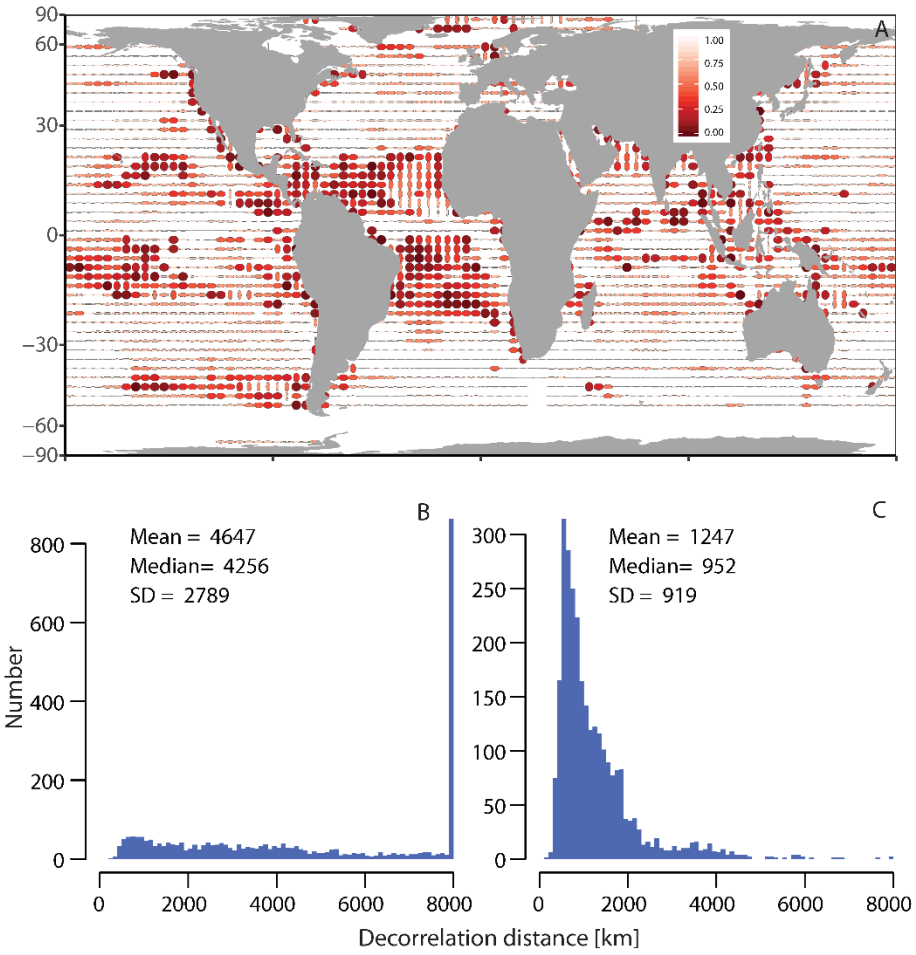

Supplementary Figure 9 | Symmetry of distance decorrelation scales. (A) Phytoplankton phenology distance decorrelation scales estimated along strictly longitudinal and latitudinal axes for each grid cell. Ellipse shape depicts the scaled symmetry of decorrelation distances. Circles and dark red depicts spatially symmetric decorrelation distances. (B-C) Statistical distribution of the phenology decorrelation distances calculated along longitude (B) and latitude (C).

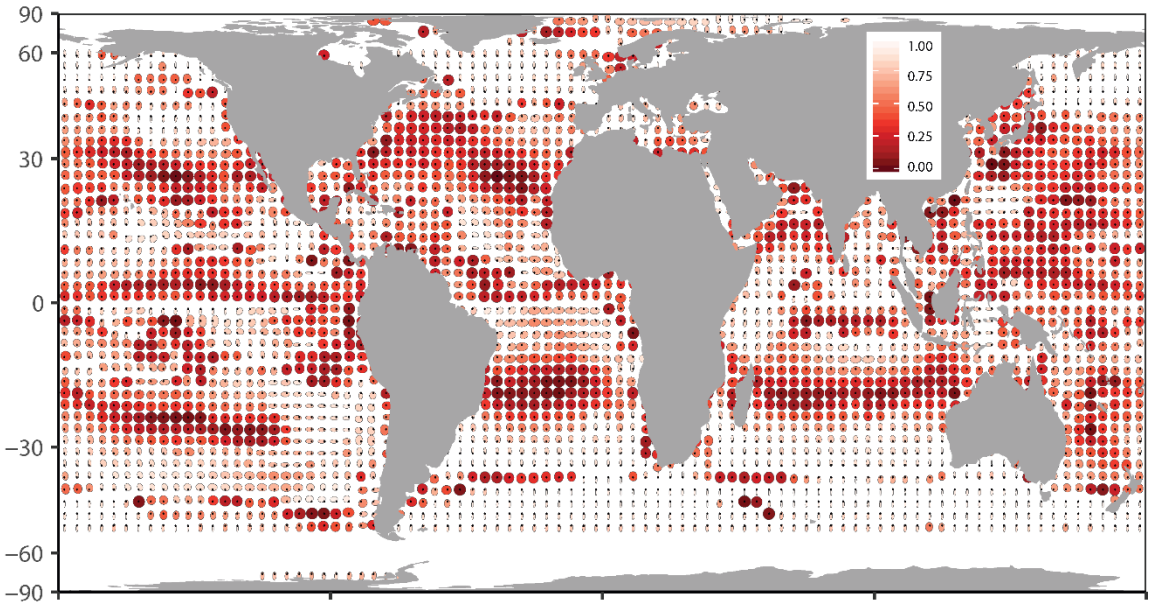

Supplementary Figure 10 | Directionality and symmetry of distance decorrelation scales. Phytoplankton phenology distance decorrelation scales estimated along cardinal (north, east, south, west) axes for each grid cell. Ellipse shape depicts the scaled symmetry of decorrelation distances in cardinal directions. The distance between the outer boundaries of the ellipses and the centers of each grid cell (black points) depicts the decorrelation scale in each cardinal direction. Circles and dark red depicts spatially symmetric decorrelation distances; more elliptical light red depicts asymmetric decorrelation distances.

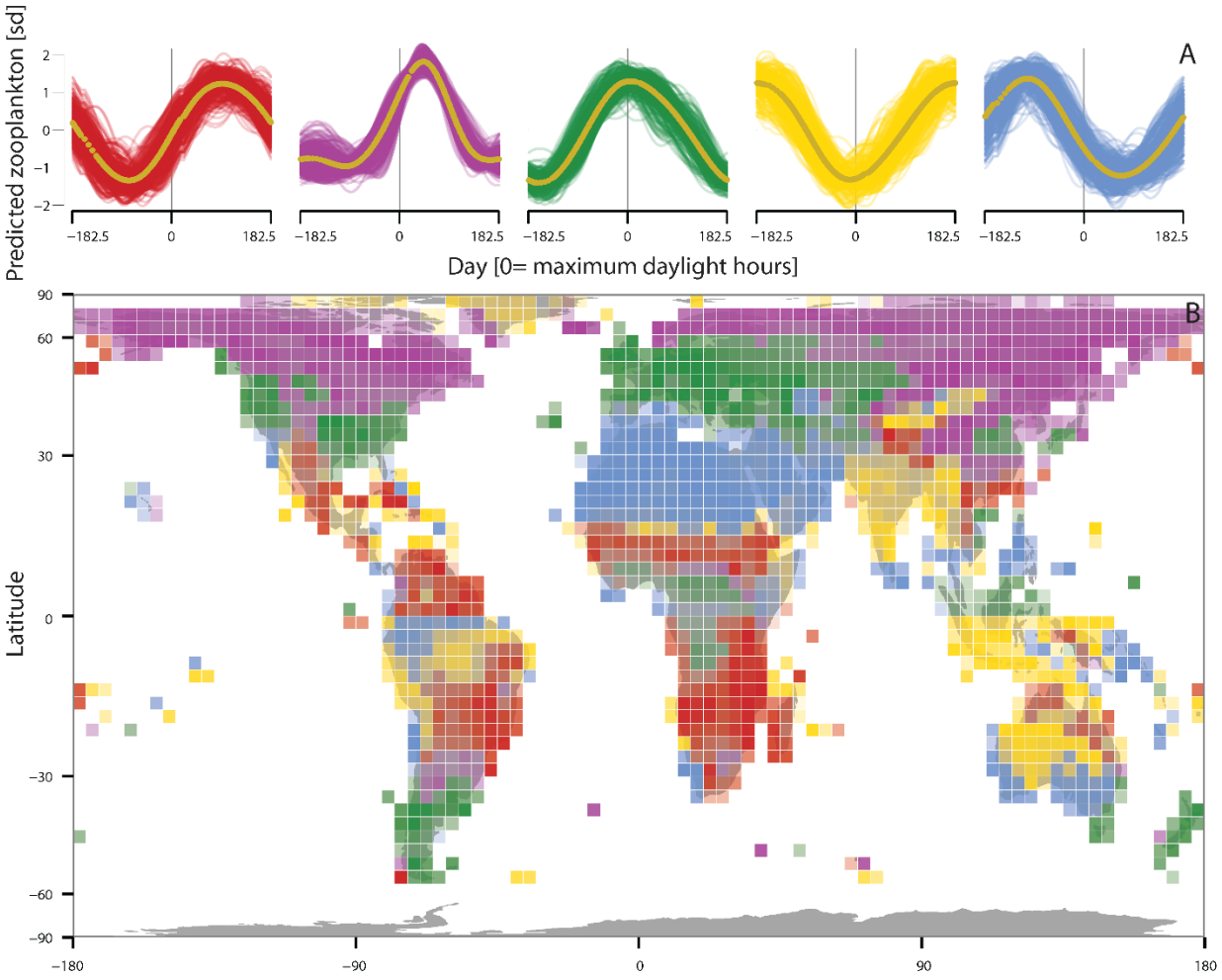

Supplementary Figure 11 | Fuzzy clustering of global land vegetation phenocycles. (A) Annual variability in standardized NDVI anomalies for each cluster. Semi-transparent colour lines are the estimated phenocycles from each grid cell. Colours identify the clusters; thick yellow lines depict the average trend for each cluster. The vertical line depicts the timing of the maximum daylight hours. (B) Spatial distribution of the phenology clusters. Colours depict the cluster membership, and transparency depicts the probability of cluster membership; opaque represents

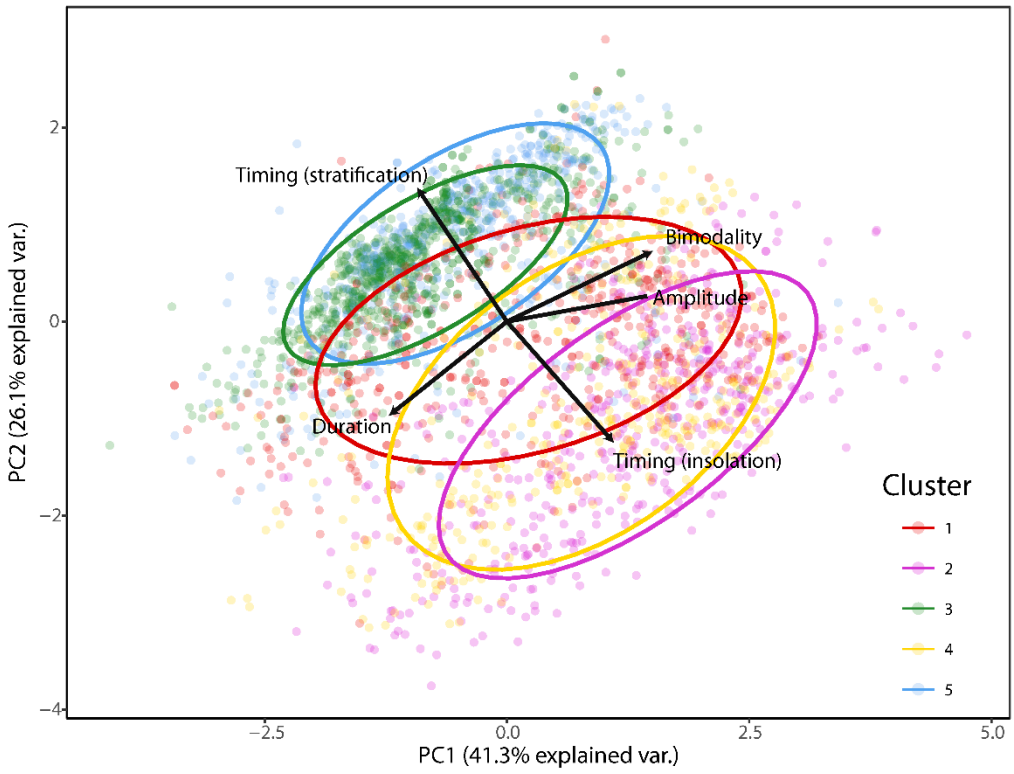

Supplementary Figure 12 | Environmental correlates of phytoplankton phenology. Principal component analysis is showing the multivariate relationship among the main phenological indices. Colours depict the five clusters identified in Figure 2.

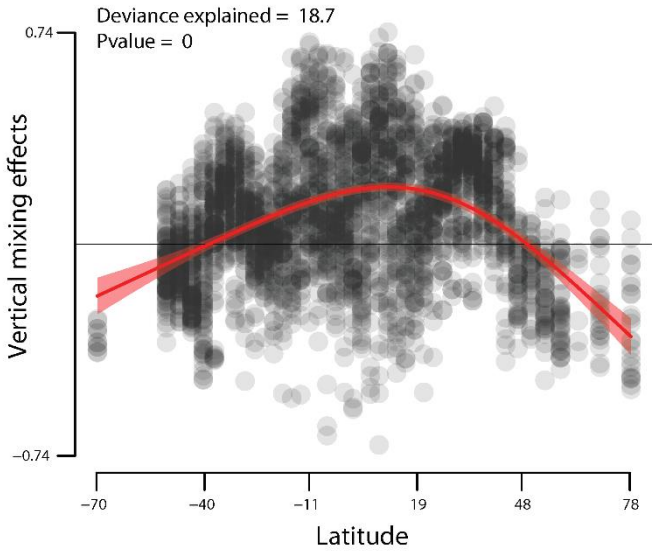

Supplementary Figure 13 | Latitudinal effects of vertical mixing on phytoplankton phenology. Red trend line and shading are the best-fitting GAM trend line and 95% CI about the trend, respectively.

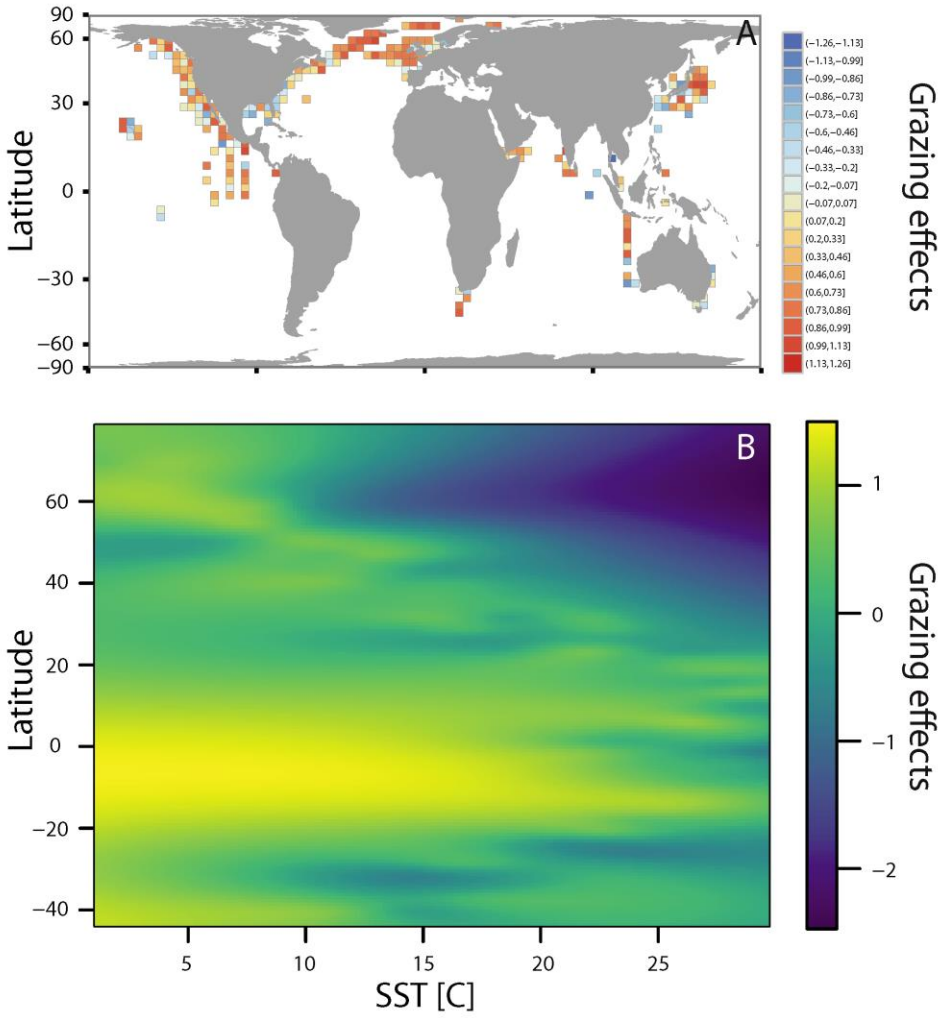

Supplementary Figure 14 | Estimated SEM effects of grazing on phytoplankton phenology cycles. (A) Spatial pattern of the grazing effects. Colours depict the direction and magnitude of the effects; dark blue depicts large negative effects, dark red depicts large positive effects. White areas depict areas where data did not permit SEM analyses of grazing effects. (B) Three-way interaction displaying variation in the grazing effects along gradients in average SST (x-axis), and latitude (y-axis). Colours depict the direction of the grazing effects; dark blue are large negative effects, and yellow and light green are positive effects.

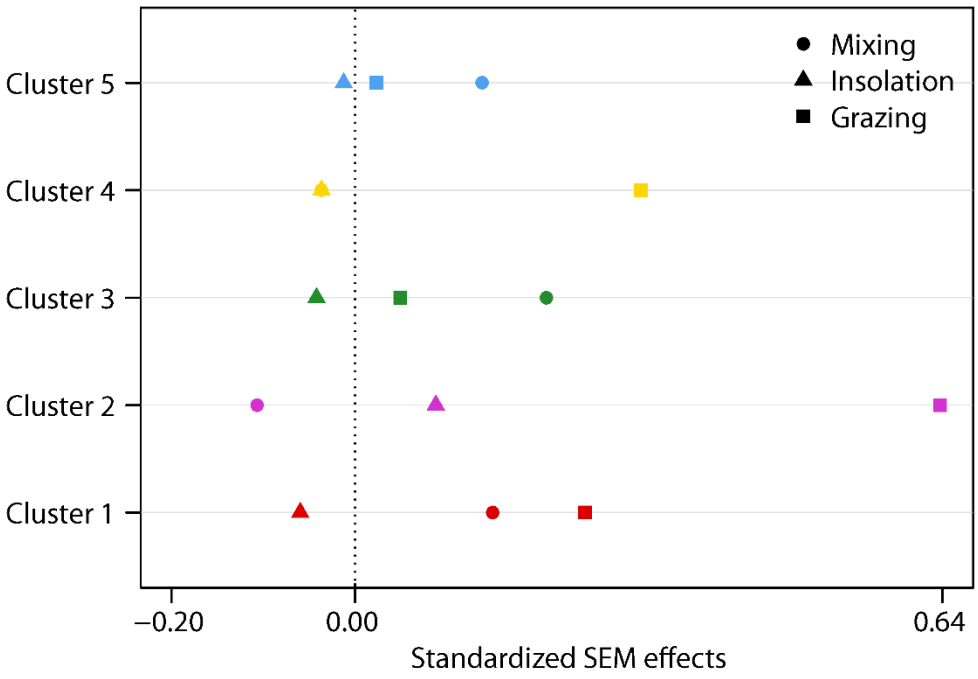

Supplementary Figure 15 | Estimated SEM effects within the five phenology clusters. The standardized SEM effects of vertical mixing, insolation and grazing are averaged within each of the the five identified clusters. Colours depict the identified clusters and symbols represent the type of SEM effects.

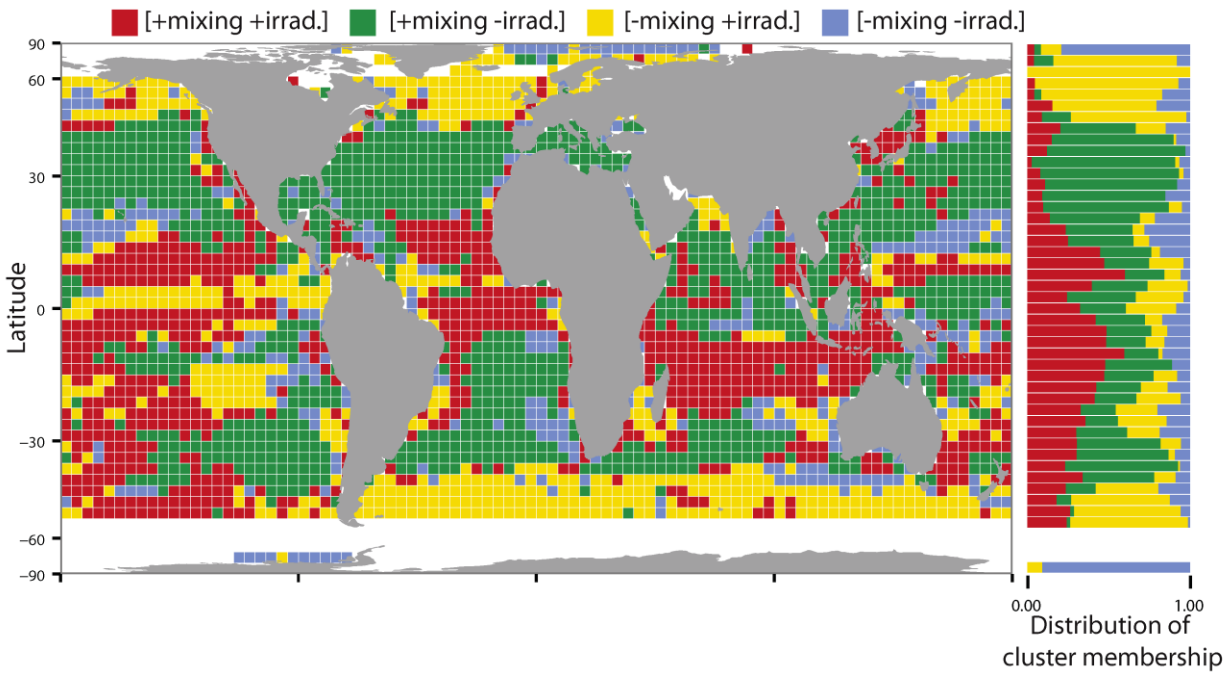

Supplementary Figure 16 | Global distribution of vertical mixing and irradiance effects on phytoplankton phenology. Red depicts cells where both mixing and irradiance effects are positive, green where mixing is positive and irradiance is negative, yellow where mixing is negative and irradiance is positive, and blue where both mixing and irradiance are negative. Barplot in right margin depicts the distribution of these clusters along latitude.

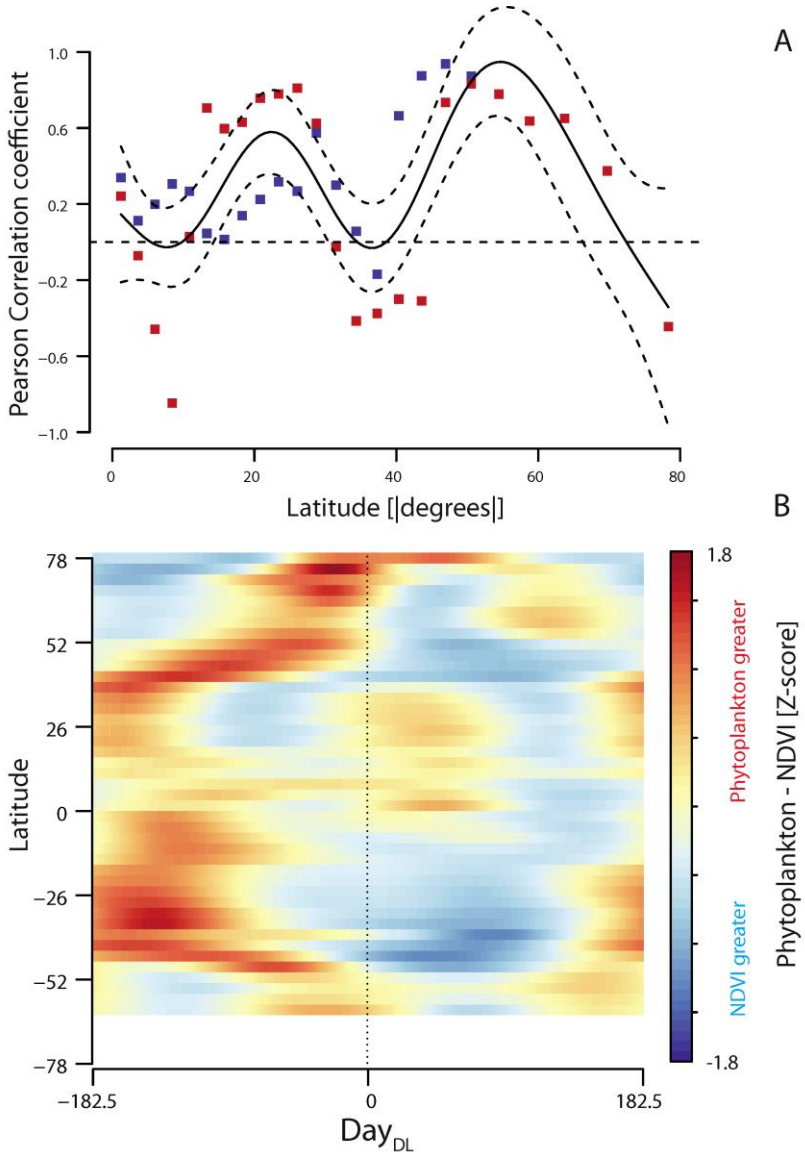

Figure S17 | Correlation between phenocycles on land and at sea as a function of latitude. (A) Colours depict the hemisphere; red are northern and blue are southern. Solid line is the best-fitting GAM trend fitted to the points and dashed lines are the 95% CI about the trend. (B) Colours depict the different between latitude averaged terrestrial and marine phenocycles. Colours depict the difference between the two (phytoplankton – NDVI); red depicts situations where phytoplankton phenocycles are greater and blue where terrestrial phenocycles are greater.